System Identification and Adaptive Tracking Control for a 3-DOF LCD Glass-handling Robot

Rong-Fong Fung* and Sin-Syun You

Department of Mechanical and Automation Engineering, National Kaohsiung First University of Science and Technology, Taiwan

(**Received** 30 November 2010; **Accepted** 14 June 2011; **Published on line** 1 September 2011)

*Corresponding author: rffung@ccms.nkfust.edu.tw

DOI: 10.5875/ausmt.v1i1.56

Abstract: In this paper, a physical model of a 3 Degree-Of-Freedom (DOF) LCD glass-handling robot driven by three Permanent Magnet Synchronous Motors (PMSMs) is established. The completely mathematical model includes two parts: the electrical equations of the three PMSMs and mechanical equations of the system in three directions. In numerical simulations, MATLAB software was employed to solve the mathematical models, while Real-coded Genetic Algorithm (RGA) was used to identify the system parameters which include those not easily measured from experiments. Numerical simulations and experimental results were compared to show the identified parameters of the mechatronic system. In the adaptive control design, Lyapunov function was employed and the external loading and unknown disturbances were considered. Two different commands of angular-displacement curve of the trapezoidal and double S speed profiles were used as the tracking trajectories for comparison. It was concluded that the double S speed profile has smaller tracking errors than those of the trapezoidal speed profile.

Keywords: 3-DOF LCD Glass-handling robot; double S speed profile; Lyapunov function; permanent magnet synchronous motors (PMSMs); Real-coded Genetic Algorithm (RGA).

1. Introduction

In recent years, flat panel displays such as liquid crystal display (LCD) and wafer have replaced the cathode ray tube (CRT) display due to their small volume, lighter weight and low power consumption. As such, the electronics industry has produced a great deal of products using this technology, like LCD-TVs, monitors, mobile displays, etc. For the LCD-TV, many LCD manufacturers have made the large size and thin film mother glass in order to meet consumers' demands. For transport of mother glasses among these equipments, the LCD glass-handling robot, stocker crane, conveyor, and automatically guided vehicle are used, with the LCD glass-handling robot as being the most essential transport device. Many dynamic models [1, 2] of mechanical systems were formulated in industrial applications. For example, Hamilton's principle was employed to derive Lagrange's equations for a LCD glass-handling robot [1] driven by a Permanent Magnet Synchronous Motor (PMSM). Fung *et al.* [2] developed the dynamic models for motor currents, angular speeds and input voltages of the PMSM driving the XY precision positioning table.

System parameters could be identified by the Real-coded Genetic Algorithm (RGA). Genetic algorithm was first defined by John Holland in 1975 and is a search process based on natural selection now being used as a tool for searching in large, poorly understood spaces that arise in many application areas of science and engineering. RGA is an optimization searching algorithm which simulates an evolution mechanism on a computer-based platform in conjunction with natural selection and genetic mechanism. The chromosomes are expressed by vectors and each element is called a gene.

The initial real-valued genes in the chromosomes are obtained through generating a sequence of real-valued variable by a randomly limited range. All chromosomes are composed of a population and are evaluated according to the pre-given evaluation index and given fitness values.

However, it is more natural to represent the genes directly as real numbers, because the method is calculated by real code and has high calculation efficiency. In uses where RGA is employed to find the identified parameters of the system, Fung and Lin [3] identified a novel 6 Degree-Of-Freedom (DOF) precision positioning table, which is assembled by two different 3-DOF precision positioning tables. Tian and Collins [4] proposed a novel trajectory planning method for a robot manipulator whose workspace includes several obstacles.

For the motion trajectory control, Hsu *et al.* [5] designed the trapezoidal and double S trajectory profiles for the electric injection molding machine during the closing operation, and the effectiveness of the Adaptive Tracking Control (ATC) was demonstrated by numerical simulations and experiments. Biagiotti and Melchiorri [6] developed the trajectory planning for automatic machines and robots. In a plant model, the system performance can be easily deteriorated by external disturbances, nonlinearities, and some parametric uncertainties due to unavoidable modeling errors. The adaptive control is able to eliminate these external disturbances and nonlinearities [7-13]. In these studies, Hu *et al.* [7] designed a modified version of the controller based on adaptive variable structure output feedback control, which satisfies the global reaching condition of sliding mode and adapts the unknown upper bounds of the lumped uncertainties and perturbations. Shanhnazi and Akbarzadeh-T [8] developed the PI-adaptive fuzzy control architecture for a class of uncertain nonlinear systems to provide robustness in the presence of large and fast but bounded uncertainties and disturbances.

Rong-Fong Fung received the Ph.D degree in Mechanical Engineering from National Taiwan University, Taiwan, in 1993. He is currently, a professor of Department of Mechanical & Automation Engineering (from Aug. 2000) and Graduate Institute of Electro-Optical Engineering (from Aug. 2004), Dean of College of Engineer (from Aug. 2010), and Chairman of Institute of Engineering Science and Technology (from Aug. 2010), National Kaohsiung First University of Science and Technology (NKFUST), Taiwan. His main research interest includes dynamics and control of opto-mechatronic systems, and equipment development of automated optical inspection (AOI) for LED and vehicle lamps. He received the Outstanding Research Award (2005, 2010, NKFUST), Outstanding Industry-Academia Cooperation Award (2010, NKFUST), Outstanding Engineering Professor Award (2006, the Chinese Mechanical Engineering Association, Taiwan), and Outstanding Research Award, 2004, NSC, Taiwan).

Sin-Syun You received the M.S. degree in Mechanical Engineering from National Kaohsiung First University of Science and Technology (NKFUST), Taiwan, in 2010. He is now serving his compulsory military duties in the army.

Chuang *et al.* [9] used the inertia-related Lyapunov function to design an adaptive controller for the motor-toggle servo mechanism. Lin *et al.* [10] formulated a robust controller with the adaptive uncertainty observer to increase the robustness of the motor drive system. Lee *et al.* [11] studied an adaptive control scheme with a pre-specified HN property for the tracking control of the permanent magnet synchronous motor (PMSM) drives. Fung and Lin [12] based on the state-space model; the adaptive backstepping control was proposed to track contour trajectories. Fung *et al.* [13] developed the adaptive backstepping fuzzy control method to compensate for the piezoelectric hysteresis and achieve motion tracking control.

This present article follows the mathematical modeling of the dynamic equations [1, 2], which include electrical and mechanical equations, and extends the 1-DOF system [1] to the 3-DOF by adding the yaw and vertical directions for real industry applications. Kinematic equations are used to describe the end point of the arm of the 3-DOF LCD glass-handling robot. The parameters are identified by the RGA method. In controller design, two tracking curves of trapezoidal and double S speed profiles are employed for the commands of the PMSMs. In the adaptive control, we consider the dynamic performance, robustness of parameter variations, trajectory-tracking errors, external loading and unknown disturbances compensation.

In this paper, the complete mechatronic formulation including the electrical and mechanical equations is performed. In control performance, it is concluded that using the double S speed profile could have a better working cycle than that of the trapezoidal speed profile. The proposed adaptive controller can compensate for the external loading and unknown disturbances, which are considered in the nonlinear time-variant mechatronic system.

2. Systems Formulation

Figure 1 shows the 3-DOF LCD glass-handling robot driven by three PMSMs. Figure 1(a) shows the side view, Figure 1(b) shows the three PMSMs, and Figure 1(c) shows the three arms from the top view. In order to complete the dynamic equations, we used both the electrical and mechanical equations to describe them.

2.1 Electrical equations

The desirable features of the PMSM are its compact structure, high air-gap flux density, high power density, high torque-to-inertia ratio, and high torque capability. The PMSM drive plays a vitally important role in motion-control applications and in the low-to-medium

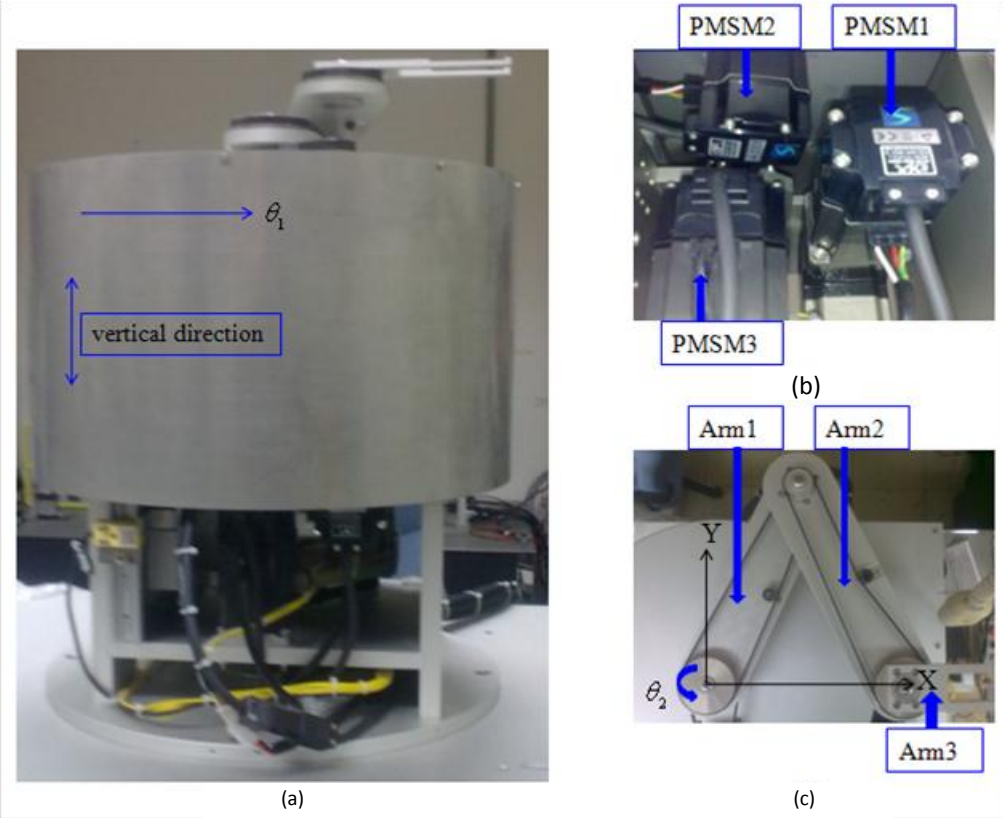

Figure 1. Three-DOF LCD glass-handling robot. (a) Side view;(b) The three PMSMs; (c) The three arms from top view.

power ranges. To achieve fast four-quadrant operation and smooth starting and acceleration, the field-oriented control is used in the design of the PMSM drive. However, its control performance is still influenced by the uncertainties of the plant, including unpredictable plant parameter variations, external loading disturbances, uncertainties and nonlinear dynamics.

The PMSM is used to drive the timing belts, screws and gears, and then to drive the mechanical system. The electrical models of the three PMSMs can be described in the rotating coordinates as follows:

$$\boldsymbol{V}_{qi} = \boldsymbol{R}_{si}\boldsymbol{i}_{qi} + \frac{d}{dt}\lambda_{qi} + \lambda_{di}\omega_{si}\,, \tag{1}$$

$$\boldsymbol{V}_{di} = \boldsymbol{R}_{si}\boldsymbol{i}_{di} + \frac{d}{dt}\lambda_{di} - \omega_{si}\lambda_{qi}\,, \tag{2}$$

where

$$\lambda_{qi} = \boldsymbol{L}_{qi}\boldsymbol{i}_{qi}\,, \tag{3}$$

$$\lambda_{di} = \boldsymbol{L}_{di}\boldsymbol{i}_{di} + \boldsymbol{L}_{mdi}\boldsymbol{I}_{fdi}\,. \tag{4}$$

The subscripts *d* and *q* represent the parameters on the *d* - and *q* -axes, and the subscript *i*=1, 2 and 3 represent the parameter in PMSM1, 2 and 3, respectively. $\boldsymbol{V}_{di}$ and $\boldsymbol{V}_{qi}$ are the stator voltages, $\boldsymbol{i}_{di}$ and $\boldsymbol{i}_{qi}$ are the stator currents, $\boldsymbol{L}_{di}$ and $\boldsymbol{L}_{qi}$ are inductances, λ_{di} and λ_{qi} are the stator flux linkages, $\boldsymbol{R}_{si}$ and ω_{si} are the stator resistances and inverter frequencies, respectively. In Equations (3) and (4), $\boldsymbol{I}_{fdi}$ and $\boldsymbol{L}_{mdi}$ are the equivalent *d*-axis magnetizing currents and inductances, respectively.

The electromagnetic torques are

$$\tau_{ei} = \frac{3}{2}p\left[\boldsymbol{L}_{mdi}\boldsymbol{I}_{fdi}\boldsymbol{i}_{qi} + \left(\boldsymbol{L}_{di} - \boldsymbol{L}_{qi}\right)\boldsymbol{i}_{di}\boldsymbol{i}_{qi}\right], \tag{5}$$

where *p* is the number of pole pairs. Equations for the motor dynamics are

$$\tau_{ei} = \tau_{mi} + \boldsymbol{B}_{mi}\omega_{ri} + \boldsymbol{J}_{mi}\dot{\omega}_{ri}\,, \tag{6}$$

where τ_{mi}, $\boldsymbol{B}_{mi}$, ω_{ri}, $\dot{\omega}_{ri}$ and $\boldsymbol{J}_{mi}$ are the load torques, damping coefficients, angular speeds, angular accelerations, moments of inertia of the rotors, respectively. In addition, the relations between the inverter frequencies (ω_{si}) and rotor angular speeds (ω_{ri}) can be expressed as

$$\omega_{si} = p\omega_{ri}\,. \tag{7}$$

The basic principle in controlling the PMSM drive is based on the field orientation. The flux position in the *d*-*q* coordinate can be determined by the shaft-position

sensor because the magnetic flux generated from the rotor permanent magnet is fixed in relation to the rotor shaft position. In Equation (5), if $\boldsymbol{i}_{di}$ =0 the *d*-axis flux linkages $\boldsymbol{\lambda}_{di}$ are fixed since $\boldsymbol{L}_{mdi}$ and $\boldsymbol{I}_{fdi}$ are constants for the surface-mounted PMSMs, and the electromagnetic torques $\boldsymbol{\tau}_{ei}$ of Equation (5) are then proportional to $\boldsymbol{i}_{qi}$, which are determined by the closed-loop control.

The rotor flux is produced in the *d*-axis only, and the current vector is generated in the *q*-axis for the field-oriented control. The generated motor torque is linearly proportional to the *q*-axis currents $\boldsymbol{i}_{qi}$, when the *d*-axis rotor flux linkages $\boldsymbol{\lambda}_{di}$ are constants, and the maximum torques per ampere will be achieved. With the implementation of field-oriented control, the electric torques of Equation (5) can be simplified as

$$\boldsymbol{\tau}_{ei} = \boldsymbol{k}_{ti}\boldsymbol{i}_{qi}\,, \tag{8}$$

$$\boldsymbol{k}_{ti} = \frac{3}{2}p\boldsymbol{L}_{mdi}\boldsymbol{I}_{fdi}\,, \tag{9}$$

where $\boldsymbol{k}_{ti}$ are the motor torque constants.

Finally, the load torques [1, 2] can be obtained by substituting Equation (8) into Equation (6) as follows:

$$\boldsymbol{\tau}_{mi} = \boldsymbol{k}_{ti}\boldsymbol{i}_{qi} - \boldsymbol{J}_{mi}\dot{\boldsymbol{\omega}}_{ri} - \boldsymbol{B}_{mi}\boldsymbol{\omega}_{ri}\,. \tag{10}$$

2.2 Mechanical equations

In the dynamic formulation, three PMSMs are independent and the timing belts are assumed rigid. The PMSM1 is used to rotate the robot in the yaw (*z*) direction, and the dynamic equation is

$$J_1\ddot{\theta}_1 + B_1\dot{\theta}_1 + K_1\theta_1 = k_{t1}i_{q1}\,, \tag{11}$$

where θ_1, $\dot{\theta}_1$, $\ddot{\theta}_1$ are the angular displacement, speed and acceleration, respectively, J_1 is the moment of inertia of the rotor, B_1 is the damping coefficient, K_1 is the equivalent stiffness, and k_{t1} is the motor torque constant of the PMSM1.

For the PMSM2, the motor is used to drive the robot, and the dynamic equation could be derived from previously published research [1] as follows:

$$\begin{aligned}&\left[J_{02} - J_{12}\cos\left(n_2\theta_2\right) + J_{m2}\right]\ddot{\theta}_2\\ &+B_{m2}\dot{\theta}_2 + \mu\sin\left(n_2\theta_2\right)\dot{\theta}_2^{\,2} = k_{t2}i_{q2}\end{aligned}\,, \tag{12}$$

Where

$$\begin{aligned}J_{02} = {} & I_1 + \left(n_2-1\right)^2 I_2 + \left(1-2n_2\right)^2 I_3 + \left(n_2-1\right)^2 I_4\\ & +4I_5 + \left(1-2n_2\right)^2 I_6 + m_2\left[l_1^{\,2} + \left(n_2-1\right)^2 b^2\right]\\ & +m_3\left[l_1^{\,2} + \left(n_2-1\right)^2 l_2^{\,2}\right] + m_4 l_1^{\,2} + m_5 l_1^{\,2}\\ & +m_6\left[l_1^{\,2} + \left(n_2-1\right)^2 l_2^{\,2}\right],\end{aligned}$$

$$J_{12} = 2\left(n_2-1\right)\left[m_2 b + \left(m_3+m_6\right)l_2\right]l_1\,,$$

$$\mu = n_2\left(n_2-1\right)\left[m_2 b + \left(m_3+m_6\right)l_2\right]l_1\,.$$

θ_2, $\dot{\theta}_2$, $\ddot{\theta}_2$ are the angular displacement, speed and acceleration of the PMSM2, respectively. n_2 is the radius ratio of the two gears that belted together in Arm 1 and it is assumed that the radius ratio in Arm 2 is also n_2. J_{m2} is the motor moment inertia of the roto. B_{m2} is the motor damping coefficient. μ is the nonlinear damping coefficient. I_1–I_3 are the moments of inertia of Arms 1–3 respectively. I_4–I_6 are the moments of inertia of Gear 2-4 respectively. m_2 and m_3 are the masses of Arms 2 and 3 respectively. m_4–m_6 are the masses of Gears 2–4 respectively. b is the moment Arm of Arm 2 with respect to the joint center of Arm 1 and Arm 2.

The PMSM3 is used to translate the robot in the vertical direction via a screw with a lead ℓ_3. The dynamic equation is

$$J_3\ddot{\theta}_3 + B_3\dot{\theta}_3 + K_3\theta_3 = k_{t3}i_{q3} - \tau_{30}\,, \tag{13}$$

where θ_3, $\dot{\theta}_3$, $\ddot{\theta}_3$ are the angular displacement, speed and acceleration, respectively, and τ_{30} is the torque due to gravity. The vertical displacement Z can be obtained as follows:

$$Z = \ell_3\frac{\theta_3}{2\pi}\,. \tag{14}$$

2.3 The combined equation

The electrical equation (1) for the three PMSMs and the dynamic equations (11-13) for the mechanical system for the 3-DOF LCD glass-handling robot can be combined into a matrix form as follows:

$$\boldsymbol{E}\dot{\boldsymbol{x}}(t) = \boldsymbol{A}\boldsymbol{x}(t) - \boldsymbol{f}(t,\theta_2) + \boldsymbol{B}\boldsymbol{u}(t) - \boldsymbol{D}_L\,, \tag{15}$$

$$\boldsymbol{y}(t) = \boldsymbol{C}\boldsymbol{x}(t)\,, \tag{16}$$

where

$$\boldsymbol{E}=\begin{bmatrix} L_{q1} & 0 & 0 & 0 & 0 & 0 & 0 & 0 & 0 \\ 0 & 1 & 0 & 0 & 0 & 0 & 0 & 0 & 0 \\ 0 & 0 & J_1 & 0 & 0 & 0 & 0 & 0 & 0 \\ 0 & 0 & 0 & L_{q2} & 0 & 0 & 0 & 0 & 0 \\ 0 & 0 & 0 & 0 & 1 & 0 & 0 & 0 & 0 \\ 0 & 0 & 0 & 0 & 0 & J_{02}+J_{m2} & 0 & 0 & 0 \\ 0 & 0 & 0 & 0 & 0 & 0 & L_{q3} & 0 & 0 \\ 0 & 0 & 0 & 0 & 0 & 0 & 0 & 1 & 0 \\ 0 & 0 & 0 & 0 & 0 & 0 & 0 & 0 & J_3 \end{bmatrix},$$

$$\boldsymbol{A}=\begin{bmatrix} -R_{s1} & 0 & -\lambda_{d1} & 0 & 0 & 0 & 0 & 0 & 0 \\ 0 & 0 & 1 & 0 & 0 & 0 & 0 & 0 & 0 \\ k_{t1} & -k_1 & -B_1 & 0 & 0 & 0 & 0 & 0 & 0 \\ 0 & 0 & 0 & -R_{s2} & 0 & -\lambda_{d2} & 0 & 0 & 0 \\ 0 & 0 & 0 & 0 & 0 & 1 & 0 & 0 & 0 \\ 0 & 0 & 0 & k_{t2} & 0 & -B_{m2} & 0 & 0 & 0 \\ 0 & 0 & 0 & 0 & 0 & 0 & -R_{s3} & 0 & -\lambda_{d3} \\ 0 & 0 & 0 & 0 & 0 & 0 & 0 & 0 & 1 \\ 0 & 0 & 0 & 0 & 0 & 0 & k_{t3} & -k_3 & -B_3 \end{bmatrix},$$

$$\boldsymbol{B}=\begin{bmatrix} 1 & 0 & 0 \\ 0 & 0 & 0 \\ 0 & 0 & 0 \\ 0 & 1 & 0 \\ 0 & 0 & 0 \\ 0 & 0 & 0 \\ 0 & 0 & 1 \\ 0 & 0 & 0 \\ 0 & 0 & 0 \end{bmatrix}, \quad \boldsymbol{C}=\begin{bmatrix} 0 & 0 & 1 & 0 & 0 & 0 & 0 & 0 & 0 \\ 0 & 0 & 0 & 0 & 0 & 1 & 0 & 0 & 0 \\ 0 & 0 & 0 & 0 & 0 & 0 & 0 & 0 & 1 \end{bmatrix},$$

$$\boldsymbol{f}(t;\theta_2)=\begin{bmatrix} 0 \\ 0 \\ 0 \\ 0 \\ 0 \\ J_{12}\cos(n_2\theta_2)-\mu\sin(n_2\theta_2)\dot{\theta}_2^{\,2} \\ 0 \\ 0 \\ 0 \end{bmatrix},$$

$$\boldsymbol{x}(t)=\begin{bmatrix} i_{q1} & \theta_1 & \dot{\theta}_1 & i_{q2} & \theta_2 & \dot{\theta}_2 & i_{q3} & \theta_3 & \dot{\theta}_3 \end{bmatrix}^T,$$

$$\boldsymbol{y}(t)=\begin{bmatrix} \dot{\theta}_1 & \dot{\theta}_2 & \dot{\theta}_3 \end{bmatrix}^T,$$

$$\boldsymbol{u}(t)=\begin{bmatrix} V_{q1} & V_{q2} & V_{q3} \end{bmatrix}^T,$$

$$\boldsymbol{D}_L=\begin{bmatrix} 0 & 0 & 0 & 0 & 0 & 0 & 0 & 0 & \tau_{30} \end{bmatrix}^T.$$

E, ***A***, ***B*** and ***C*** are the constant matrices of the system parameters. ***x***(*t*) and ***y***(*t*) are the state and output variable vectors, respectively. ***u***(t) is the control voltage vector, $\boldsymbol{f}(t,\theta_2)$ is the nonlinear part of the dynamic equation from PMSM2, and $\boldsymbol{D}_L$ is the torque due to gravity. The parameters in Equation (15) are to be identified in the following section. Equations (15) and (16) are used to design the adaptive control in Section 5.

3. Identification based on RGA — Fitness function

This study adopts the RGA to identify the system parameters. Through the RGA identification, all unknown parameters of the electrical and mechanical equations were identified. The detailed parameters are listed in Table 1. There are seven parameters for PMSM1, nine parameters for PMSM2 and eight parameters for PMSM3. Therefore, a total of 24 parameters in Equation (15) are to be identified simultaneously. The procedure of identification based on the RGA is the same as [1-3].

Since Equation (15) is a set of ordinary differential equations, the fitness function [1-3] must include total summation of the errors during the operation time and is designed as follows:

$$\boldsymbol{F}(parameters)=\frac{1}{\sum_{j=1}^{N}\left(\boldsymbol{E}_j^2\right)}, \tag{17}$$

$$\boldsymbol{E}_j=\boldsymbol{\theta}^{(j)}-\boldsymbol{\theta}^{*(j)}, \tag{18}$$

where N is the total number of sampling times in numerical simulations, the superscripts (j) and *(j) represent the experimental and simulation values at the j^{th} sampling time, respectively. $\boldsymbol{E}_j$ represents the errors of the angular displacements for PMSMs.

This fitness function (17) converges about 20 generations (not shown here) for the mechatronic system, and the 24 parameters are identified and shown in Table 1.

4. Motion Profile Design

4.1 Kinematic equation

In order to describe the kinematic equation of the 3-DOF LCD glass-handling robot, the position vector $\vec{r}_3$ of Arm 3 in Figure 5(a) should be defined. This position vector indicates the end point of the robot, and is the resultant position due to three angular departments (θ_i, $i=1, 2, 3$), which rotate by three PMSMs.

Table 1. System parameters of the 3-DOF LCD glass-handling robot.

Electrical equations	Feasible domains	Identified values	Mechanical equations	Feasible domains	Identified values
R_{s1} (Ω)	0.017-0.0185	0.0180	J_1 (kg-m^2)	0.0001-0.001	0.0008
R_{s2} (Ω)	0.017-0.0185	0.0182	J_{02} (kg-m^2)	0.001-0.1	0.0030
R_{s3} (Ω)	0.017-0.0185	0.0177	J_{12} (kg-m^2)	0.001-0.1	0.0400
L_{q1} (H)	0.016-0.02	0.1785	J_{m2} (kg-m^2)	0.0001-0.01	0.00012
L_{q2} (H)	0.016-0.02	0.1860	J_3 (kg-m^2)	0.001-0.05	0.0100
L_{q3} (H)	0.016-0.02	0.1920	B_1 (kgm-rad)	0.0001-0.05	0.0170
λ_{d1}	0.01-0.03	0.0184	B_{m2} (kgm-rad)	0.0001-0.05	0.0002
λ_{d2}	0.01-0.03	0.0210	B_3 (kgm-rad)	0.0005-0.01	0.0081
λ_{d3}	0.01-0.03	0.0205	K_1 (kgm^2-rad)	0.001-0.05	0.0012
k_{t1} (kgm/A)	0.88-0.93	0.8950	K_3 (kgm^2-rad)	0.001-0.05	0.0122
k_{t2} (kgm/A)	0.88-0.93	0.9014	μ	0.1-5	2
k_{t3} (kgm/A)	0.88-0.93	0.9220	m_3	0.1-20	3.7

4.2 Trapezoidal speed profile

A very common method [4, 5] to obtain trajectories with a continuous speed profile is to use linear motions with parabolic blends, where the trajectories can be characterized by the typical trapezoidal speed profiles. In this case, a motion is defined by assigning the initial and final time instants as t_0 and t_1 and their conditions on displacement and speed at t_0 and t_1. From a mathematical point of view, the problem is then to find a function $\boldsymbol{\theta} = \boldsymbol{\theta}(t),\ t \in [t_0, t_1]$, where $\boldsymbol{\theta}(t)$ is the profile of angular displacements such that the given conditions are satisfied.

The trapezoidal trajectories are divided into three parts: acceleration phase, constant speed phase and deceleration phase. The detailed mathematical descriptions of displacements and speeds can be seen in [5, 6].

4.3 Double S speed profile

A trapezoidal speed profile presents a discontinuous acceleration. For this reason, this kind trajectory may generate efforts and stresses on mechanical systems and may result in detrimental or generate undesired vibration effects. Therefore, a smoother motion profile can be defined, for example by adopting a continuous, linear piece-wise, speed profile. In this manner, the resulting speed profile is composed by linear segments connected by parabolic blends. The shape of the speed profile is the reason of the name double S for this trajectory [6], known also as bell trajectory or seven-segment trajectory. It is composed by several tracts with constant jerk, and the detailed mathematical description of displacements and speeds can be seen in [6].

5. Adaptive Controller Design

In order to achieve good tracking control of the robot actuated by three PMSMs, the adaptive control [7] is established here, with the control variable defined as follows:

$$\boldsymbol{z}(t) = \boldsymbol{G}\boldsymbol{x}(t), \tag{19}$$

where $\boldsymbol{z}(t) = [\omega_1 \quad \omega_2 \quad \omega_3]^T$ is a vector of control variables and $\boldsymbol{G} \in R^{3\times 9}$. Equation (15) can be rewritten as follows:

$$\dot{\boldsymbol{x}}(t) = \boldsymbol{a}\boldsymbol{x}(t) + \boldsymbol{b}\boldsymbol{u}(t) - \boldsymbol{N}(t, \theta_2) - \boldsymbol{d}(t), \tag{20}$$

where $\boldsymbol{a} = \boldsymbol{E}^{-1}\boldsymbol{A}$, $\boldsymbol{b} = \boldsymbol{E}^{-1}\boldsymbol{B}$ are parameter matrices, $\boldsymbol{N}(t, \theta_2) = \boldsymbol{E}^{-1}\boldsymbol{f}(t, \theta_2)$, and $\boldsymbol{d}(t) = \boldsymbol{E}^{-1}(\boldsymbol{D}_L + \boldsymbol{D}_{dis}(t))$ is the non-constant disturbance, where the unknown disturbance $\boldsymbol{D}_{dis}(t)$ is added. We set $\Delta\boldsymbol{a}$ and $\Delta\boldsymbol{b}$ are the parameter variations of $\boldsymbol{a}$ and $\boldsymbol{b}$, respectively, and illustrate $\boldsymbol{d}(t)$ as follows:

$$\boldsymbol{d}(t) = \boldsymbol{E}^{-1}[\Delta\boldsymbol{a}\boldsymbol{x}(t) + \Delta\boldsymbol{b}\boldsymbol{u}(t) + \boldsymbol{D}_L + \boldsymbol{D}_{dis}(t)], \tag{21}$$

Following [8], we define the PI structure via the following two assumptions:

Assumption 1: We define $\boldsymbol{d}(t)$ as bounded by an unknown constant D,

$$|\boldsymbol{d}(t)| \le \mathrm{D}. \tag{22}$$

Assumption 2: We define PI structure of $\boldsymbol{d}(t)$ as follows:

$$\boldsymbol{d}(t) = \boldsymbol{d}_P\boldsymbol{e}_i + \boldsymbol{d}_I\int \boldsymbol{e}_i dt + \boldsymbol{d}_D\boldsymbol{sgn}(\boldsymbol{e}_i), \tag{23}$$

$$sgn(e_i)=\begin{cases}1 & e_i>0\\ -1 & e_i<0\end{cases}, \tag{24}$$

where $\boldsymbol{d}_p, \boldsymbol{d}_I, \boldsymbol{d}_D \in R^{3\times1}$ are constant vectors.

The method proposed in this paper is motivated by the adaptive control, which is defined by the adaptive law via Lyapunov function. Let us first follow [9-13] and consider the first-order liner time-invariant plant as shown in Equation (24).

We design the adaptive controller as follows:

$$\boldsymbol{u}(t)=\boldsymbol{u}_1(t)+\boldsymbol{u}_2(t)+\boldsymbol{u}_3(t), \tag{25}$$

where $\boldsymbol{u}_1(t)$ is used to control the system state, $\boldsymbol{u}_2(t)$ is used to eliminate the nonlinear part of PMSM2 and $\boldsymbol{u}_3(t)$ is used to eliminate the external loading and unknown disturbance.

The controllers are designed as follows:

$$\boldsymbol{u}_1(t)=-\boldsymbol{b}^*\boldsymbol{I}_\alpha\hat{\boldsymbol{\alpha}}^T\boldsymbol{z}(t)+\boldsymbol{b}^*\boldsymbol{G}^*(\lambda\ \boldsymbol{e}_i+\dot{\omega}^*), \tag{26}$$

$$\boldsymbol{u}_2(t)=\boldsymbol{b}^*\boldsymbol{N}(t;\theta_2), \tag{27}$$

$$\boldsymbol{u}_3(t)=\boldsymbol{I}_d\left[\boldsymbol{d}_p^T\boldsymbol{e}_i+\boldsymbol{d}_I^T\int\boldsymbol{e}_i dt+\boldsymbol{d}_D^T\boldsymbol{sgn}(\boldsymbol{e}_i)\right], \tag{28}$$

where $\lambda\in R^{3\times3}$, $\boldsymbol{I}_\alpha\in R^{9\times1}$, $\boldsymbol{I}_d\in R^{3\times1}$ are constant vectors, $\boldsymbol{\alpha}=\boldsymbol{\alpha}^*\boldsymbol{G}=\boldsymbol{I}_\alpha\boldsymbol{\alpha}^T\boldsymbol{G}$, $\boldsymbol{b}^*=\boldsymbol{b}^T(\boldsymbol{b}\boldsymbol{b}^T)^{-1}$ and $\boldsymbol{G}^*=\boldsymbol{G}^T(\boldsymbol{G}\boldsymbol{G}^T)^{-1}$ are constant matrices, $\hat{\boldsymbol{\alpha}}\in R^{3\times1}$ and $\hat{\boldsymbol{d}}_p, \hat{\boldsymbol{d}}_I, \hat{\boldsymbol{d}}_D\in R^{3\times1}$ are the estimations of the unknown parameters $\boldsymbol{\alpha}$, and $\boldsymbol{d}_p, \boldsymbol{d}_I, \boldsymbol{d}_D$, respectively. To develop the adaptive laws for $\boldsymbol{\alpha}$ and $\boldsymbol{d}_p, \boldsymbol{d}_I, \boldsymbol{d}_D$, their parameter errors: $\tilde{\boldsymbol{\alpha}}=\hat{\boldsymbol{\alpha}}-\boldsymbol{\alpha}$, $\tilde{\boldsymbol{d}}_p=\hat{\boldsymbol{d}}_p-\boldsymbol{d}_p$, $\tilde{\boldsymbol{d}}_I=\hat{\boldsymbol{d}}_I-\boldsymbol{d}_I$ and $\tilde{\boldsymbol{d}}_D=\hat{\boldsymbol{d}}_D-\boldsymbol{d}_D$ are needed.

Let $\boldsymbol{e}_i(t)$ and $\dot{\boldsymbol{e}}_i(t)$, i=1, 2, 3, be the errors of angular displacements and angular speeds, respectively, then the error equations ($\boldsymbol{s}_i$, i=1, 2, 3) are defined as follows:

$$\boldsymbol{s}=\lambda\boldsymbol{e}_i+\dot{\boldsymbol{e}}_i, \tag{29}$$

where $\lambda=diag\left[\lambda_1\ \ \lambda_2\ \ \lambda_3\right]$ is a positive matrix, $\boldsymbol{e}_i=\boldsymbol{\theta}_i-\boldsymbol{\theta}_i^*$ and $\dot{\boldsymbol{e}}_i=\boldsymbol{\omega}_i-\boldsymbol{\omega}_i^*$.

The error dynamics [9] of the system equation (20) is

$$\dot{\boldsymbol{s}}=\lambda\dot{\boldsymbol{e}}_i+\ddot{\boldsymbol{e}}_i, \tag{30}$$

The global asymptotic stability of Equation (20) can be guaranteed by using the adaptive laws [10-13] and Lyapunov function defined as

$$\begin{aligned}2\boldsymbol{V}=&\boldsymbol{s}^T\boldsymbol{h}\boldsymbol{s}+\tilde{\boldsymbol{\alpha}}^T\boldsymbol{\gamma}_1^{-1}\tilde{\boldsymbol{\alpha}}+\tilde{\boldsymbol{d}}_p{}^T\boldsymbol{\gamma}_2^{-1}\tilde{\boldsymbol{d}}_p\\&+\tilde{\boldsymbol{d}}_I{}^T\boldsymbol{\gamma}_3^{-1}\tilde{\boldsymbol{d}}_I+\tilde{\boldsymbol{d}}_D{}^T\boldsymbol{\gamma}_4^{-1}\tilde{\boldsymbol{d}}_D\end{aligned}. \tag{31}$$

By taking the time derivative of Lyapunov function (31), we have

$$\begin{aligned}\dot{\boldsymbol{V}}=&\boldsymbol{s}^T\boldsymbol{h}\dot{\boldsymbol{s}}+\tilde{\boldsymbol{\alpha}}^T\boldsymbol{\gamma}_1^{-1}\dot{\tilde{\boldsymbol{\alpha}}}+\tilde{\boldsymbol{d}}_p{}^T\boldsymbol{\gamma}_2^{-1}\dot{\tilde{\boldsymbol{d}}}_p\\&+\tilde{\boldsymbol{d}}_I{}^T\boldsymbol{\gamma}_3^{-1}\dot{\tilde{\boldsymbol{d}}}_I+\tilde{\boldsymbol{d}}_D{}^T\boldsymbol{\gamma}_4^{-1}\dot{\tilde{\boldsymbol{d}}}_D\end{aligned}, \tag{32}$$

where $\boldsymbol{e}_c(t)=\left[e_i(t)\ \ \tilde{\alpha}(t)\ \ \tilde{d}_P(t)\ \ \tilde{d}_I(t)\ \ \tilde{d}_D(t)\right]^T$, $\boldsymbol{\gamma}_1, \boldsymbol{\gamma}_2, \boldsymbol{\gamma}_3, \boldsymbol{\gamma}_4\in R^{3\times3}$ are constant matrices, γ_{n1} and $\gamma_{n2}\in R$ are constant values. $\boldsymbol{h}\in R^{3\times3}$ is a constant matrix such that $\boldsymbol{h}=\boldsymbol{h}^T>0$ and satisfies

$$\boldsymbol{h}\lambda+\lambda^T\boldsymbol{h}=-\boldsymbol{Q}, \tag{33}$$

for any chosen constant matrix $\boldsymbol{Q}\in R^{3\times3}$ such that $\boldsymbol{Q}=\boldsymbol{Q}^T>0$. From Equation (32), we have $\dot{\boldsymbol{V}}(\boldsymbol{e}_c(t))=-\boldsymbol{s}^T(t)\boldsymbol{Q}\boldsymbol{s}\ (t)\le0$ by using the fact that $\dot{\tilde{\boldsymbol{\alpha}}}=\dot{\hat{\boldsymbol{\alpha}}}$, $\dot{\tilde{\boldsymbol{d}}}_p=\dot{\hat{\boldsymbol{d}}}_p$, $\dot{\tilde{\boldsymbol{d}}}_I=\dot{\hat{\boldsymbol{d}}}_I$ and $\dot{\tilde{\boldsymbol{d}}}_D=\dot{\hat{\boldsymbol{d}}}_D$. The adaptive laws are as follows:

$$\dot{\hat{\boldsymbol{\alpha}}}=-\boldsymbol{s}^T\boldsymbol{h}\boldsymbol{G}\boldsymbol{I}_\alpha\boldsymbol{\gamma}_1\boldsymbol{G}^{*T}z(t), \tag{34}$$

$$\dot{\hat{\boldsymbol{d}}}_p=-\boldsymbol{s}^T\boldsymbol{h}\boldsymbol{G}\boldsymbol{b}\boldsymbol{\gamma}_2\boldsymbol{e}_i, \tag{35}$$

$$\dot{\hat{\boldsymbol{d}}}_I=-\boldsymbol{s}^T\boldsymbol{h}\boldsymbol{G}\boldsymbol{b}\boldsymbol{\gamma}_3\int\boldsymbol{e}_i dt, \tag{36}$$

$$\dot{\hat{\boldsymbol{d}}}_D=-\boldsymbol{s}^T\boldsymbol{h}\boldsymbol{G}\boldsymbol{b}\boldsymbol{\gamma}_4\boldsymbol{e}_i\boldsymbol{sgn}(\boldsymbol{e}_i)\ . \tag{37}$$

6. Numerical Simulations and Experimental Results

6.1 Numerical simulations

In order to obtain numerical simulations, Runge-Kutta method [1] with tolerance error 10^{-6} was employed to simulate the variations of angular displacements θ_1, θ_2, and θ_3. By using the RGA method to identify system parameters as shown in Table 1, and substituting the assigned and identified parameters into dynamic equations (15, 16), we can obtain the compared numerical simulations (not shown here) by the commercial MATLAB software. It was found that the response errors are below ±0.5 %, ±1.5 %, and ±1.0 % for PMSM1, PMSM2 and PMSM3, respectively. The RGA method was thusly validated as feasible for parameter identification of the 3-DOF LCD glass-handling robot.

By using these identified parameters as shown in Table 1, the dynamic responses by numerical simulation

can be obtained. The comparisons between the experimental and identified results of the angular displacements are shown in Figure 2. The input voltage as shown in Figure 2(a) is $0.25\sin 0.5t + 0.05\sin 5t$ with two different frequencies to drive the PMSMs. For the PMSM drive, we set i_{di}=0, i=1, 2, 3 thus the d-axis flux linkages λ_{di}, i=1, 2, 3 are fixed. The rotor flux is produced in the d-axis only and the current vector is generated in the q-axis for the field-oriented control.

In numerical simulations of the proposed adaptive controllers, Runge–Kutta method [1] with tolerance error 10^{-6} was also employed with MATLAB software. From Equation (25), it is known that the adaptive control needs 17 gain values of $\hat{\boldsymbol{\alpha}}^T = [\hat{\alpha}_{11} \quad \hat{\alpha}_{12} \quad \hat{\alpha}_{13}]$, $\boldsymbol{h} = diag[h_1 \quad h_2 \quad h_3]$, $\hat{\boldsymbol{d}}_p^T = [\hat{d}_{p1} \quad \hat{d}_{p2} \quad \hat{d}_{p3}]$, $\hat{\boldsymbol{d}}_I^T = [\hat{d}_{I1} \quad \hat{d}_{I2} \quad \hat{d}_{I3}]$ and $\hat{\boldsymbol{d}}_D^T = [\hat{d}_{D1} \quad \hat{d}_{D2} \quad \hat{d}_{D3}]$ in $\boldsymbol{V}_{qi}$. The gain values are adjusted by adaptive laws, and the block diagram of the adaptive control is shown in Figure 3, where the constant vectors and values are

$$\gamma_1 = [100\times10^{-4} \quad 5\times10^{-4} \quad 3\times10^{-4}],$$
$$\gamma_2 = [10\times10^{-4} \quad 50\times10^{-4} \quad 70\times10^{-4}],$$
$$\gamma_3 = [25\times10^{-4} \quad 20\times10^{-4} \quad 75\times10^{-4}],$$
$$\gamma_4 = [2\times10^{-4} \quad 2\times10^{-4} \quad 2\times10^{-4}]$$
$$\boldsymbol{\eta} = diag(h_1, h_2, h_3) = diag(10, 15, 5),$$
$$\boldsymbol{\lambda} = diag(0.85, 0.7, 0.75), \text{ and } D = 100.$$

By setting these values into $\dot{\hat{\boldsymbol{\alpha}}}$, $\dot{\hat{\boldsymbol{d}}}_p$, $\dot{\hat{\boldsymbol{d}}}_I$, $\dot{\hat{\boldsymbol{d}}}_D$, $\boldsymbol{\lambda}$ and $\boldsymbol{h}$ of adaptive laws of Equations (34-37), we obtain the adaptive control of Equation (25).

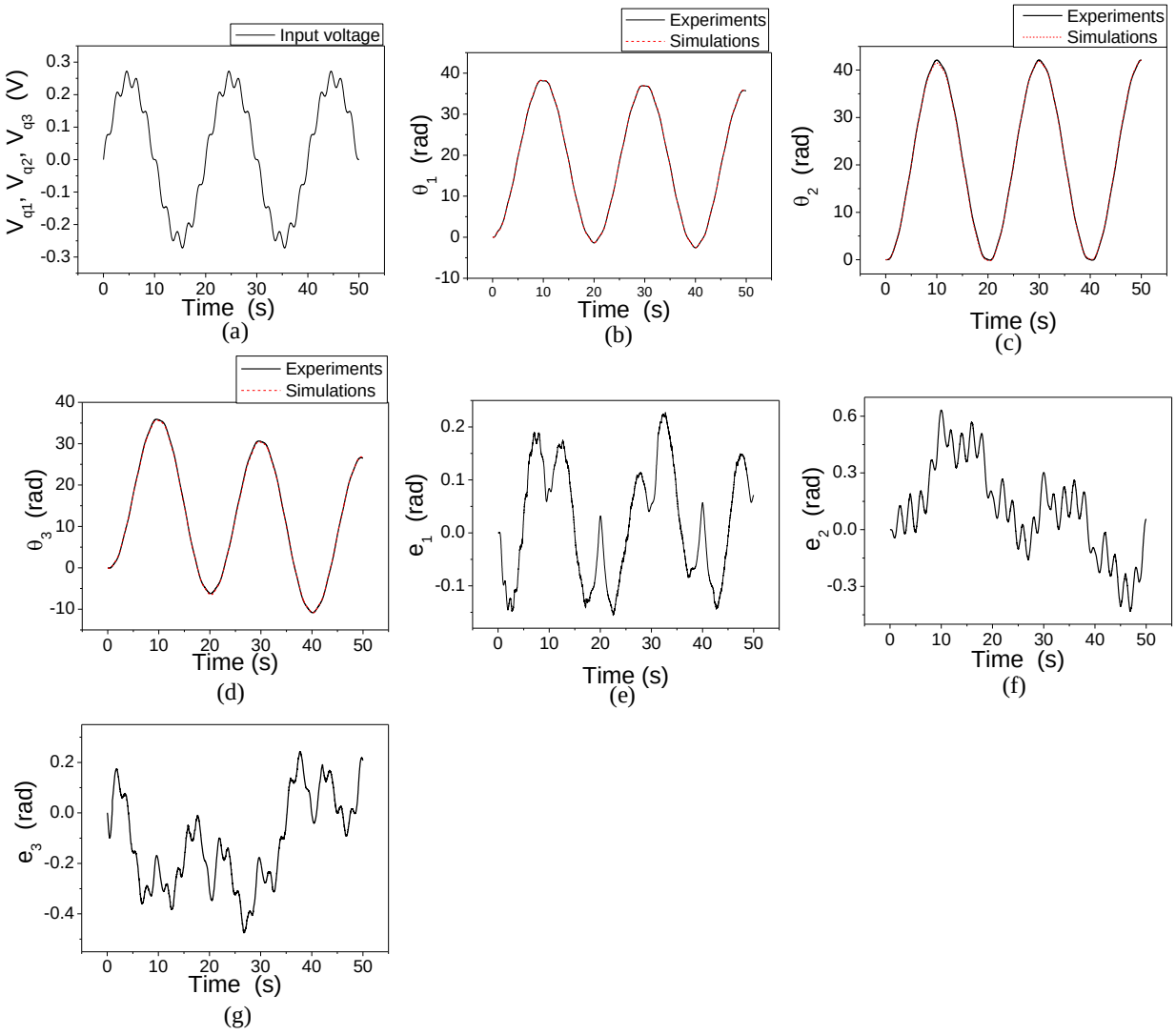

Figure 2. Comparisons between the numerical simulations and experimental results for the three PMSMs. (a) Input voltages. (b-d) Angular displacements. (e-g) Angular-displacement errors.

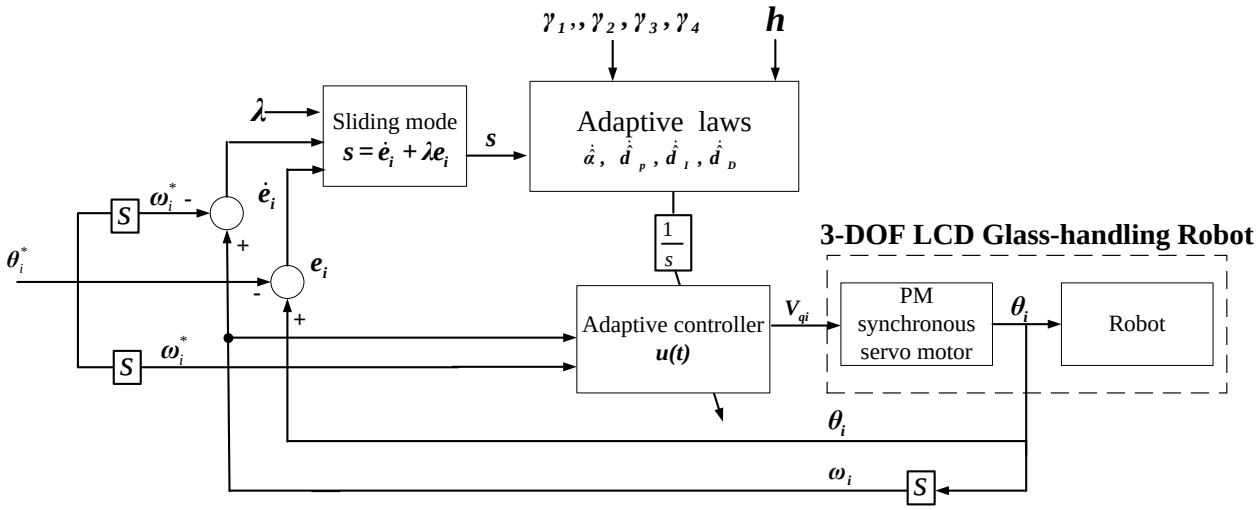

Figure 3. Block diagram of the proposed adaptive control.

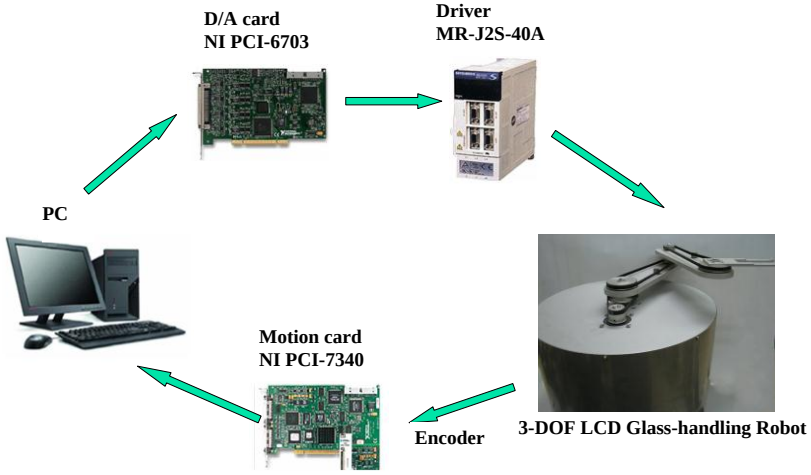

Figure .4 Experimental setup.

6.2 *Experimental setup*

An experimental setup of the 3-DOF LCD glass-handling robot is shown in Figure 4, where three PMSMs were used as actuators. The Japanese-made PMSM with MITSUBISHI HC-KFS series, and the specifications include a rated output of 400 W and rated rotation speed of 3000 rpm. The waveform of the input voltage is generated by LabVIEW software, which is a Windows supported graphical programming language. The D/A converter (NI PCI-6052) with a resolution of 12 bits is used to transform the voltage waveform to the PMSM drive with MITSUBISHI HC-KFS series, and reads the voltage of the potential meter. The encoder (MR-J2S) signal is transformed from the A/D converter to the motion card (NI PCI-7344), which will read the digital single of PMSM's encoders. By using LabVIEW software, the human machine interface (HMI) is also developed in Figure 4. The related calculation of the proposed controller is handled within the HMI.

In order to measure the angular displacements of the PMSMs, the interface device is implemented by a motion control card (NI PCI-7344) and an A/D card (NI PCI-6052), which can measure angles with a sampling time $\Delta t = 0.001$ sec. In order for system identification, we give the input voltages $0.25\sin 0.5t + 0.05\sin 5t$ to drive PMSMs, and use the PC to store angular displacements of the PMSMs.

The trapezoidal and double S speed profiles of angular displacements [6] are used to validate the proposed control method. They are designed for all three PMSMs, but with different time durations. Figure 5(a) shows the three arms in the X-Y coordinates, while Figure 5(b) shows three commands for the corresponding three PMSMs, and is the complete working cycle for duration time of nine seconds. There are eight steps included in Figure 5(a). The first graphic of Figure 5(b) is for PMSM 2 rotating the three arms and the position vector $\vec{r}_3$ moves on the *x* axis. The second and third graphics of Figure 5(b) are for the PMSMs rotating in the yaw direction and translating in the vertical direction, respectively.

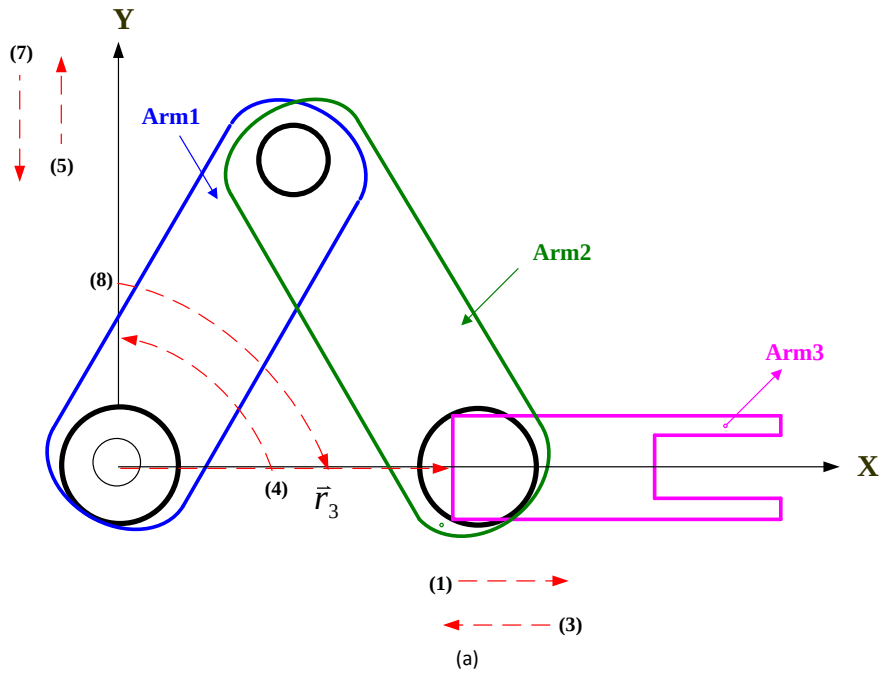

(a)

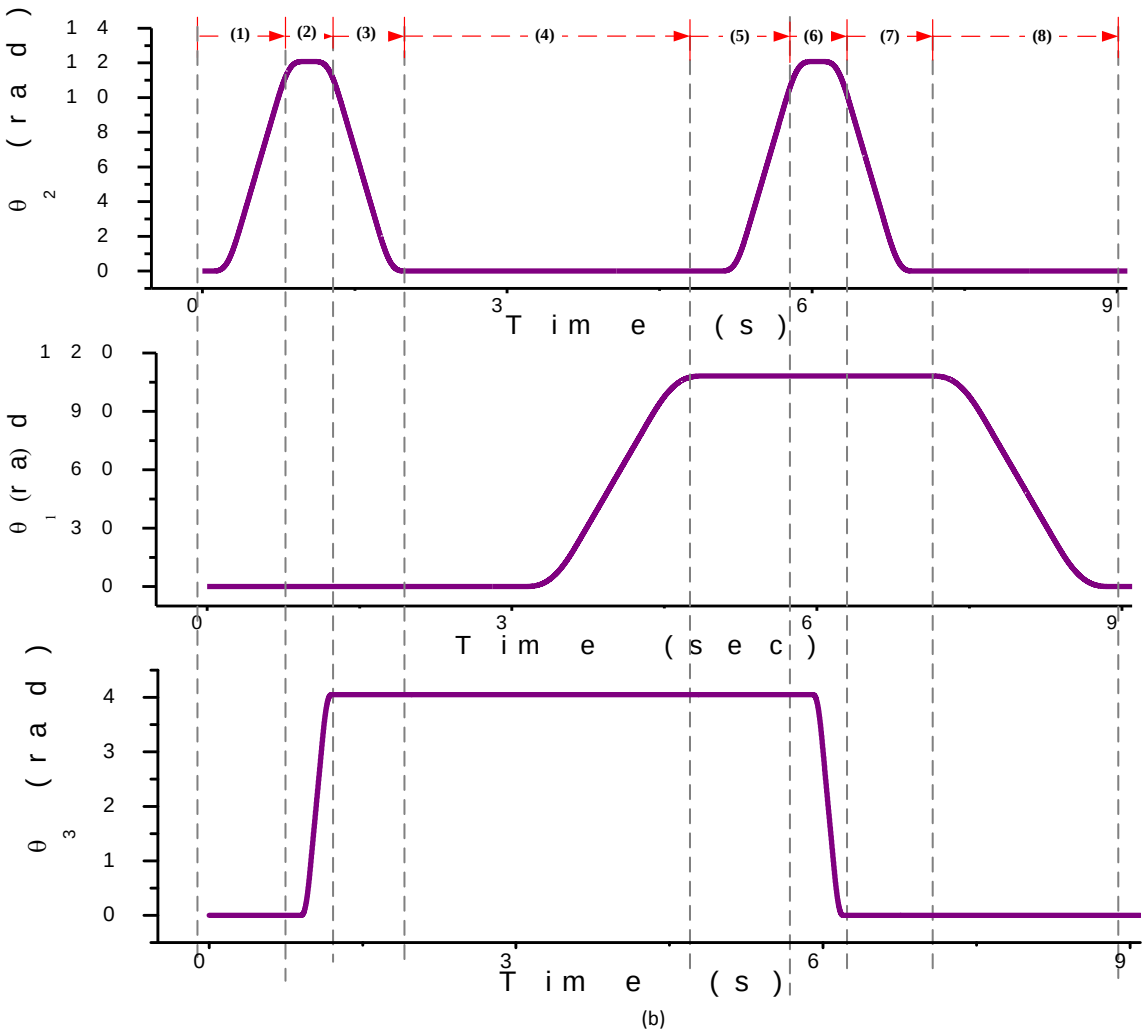

(b)

Figure 5. Complete working cycle of the 3-DOF glass-handing robot. (a) Physical model of a LCD glass-handing robot. (b) Angular-displacement commands for the three PMSMs.

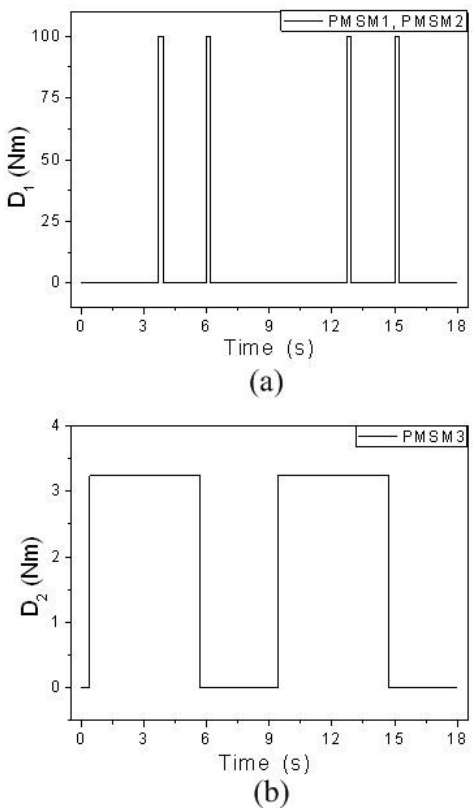

Figure 6. Torque disturbances in the numerical simulations. (a) Assigning D1 (100 Nm) to PMSM1 and PMSM2. (b) Assigning D2 (3.3 Nm) to PMSM3.

6.3 Comparisons between numerical simulations and experimental results

In order for comparisons, the results are performed for two working cycles, and each cycle takes nine seconds. In numerical simulations, Figure 6 shows the external loading and unknown disturbances added to the system. Figure 6(a) shows the external loading resulting in the jumping for the PMSM1 and PMSM2. Figure 6(b) shows the effect of external loading in the step of the PMSM3. Two examples of jumping torques are shown in the PMSM1 and PMSM2, but their time durations are much shorter than with the PMSM3.

Figure 7 shows the comparison results of numerical simulations between the trapezoidal and double S speed profiles. Figures 7(a-c) show the control voltages of the three PMSMs, and it is seen that the trapezoidal speed profile has more jumping phenomenon than that of the double S speed profile. Figures 7(d-f) show the angular displacements of the three PMSMs, and Figures 7(g-i) show their angular speeds. In these figures it is seen that the designed controller can be used to control the robot system, and the response results of θ_1, θ_2 and θ_3 are well in agreement with the commands in the first working cycle, and they are convergent in the second working cycle.

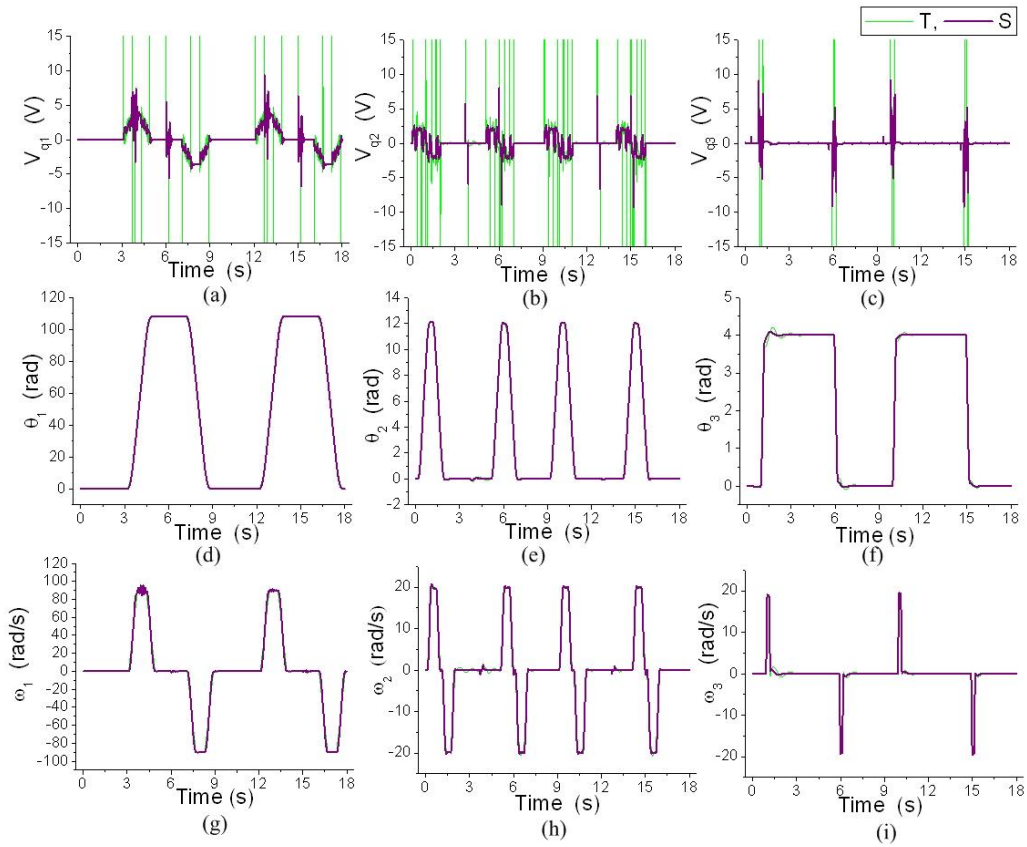

Figure 7. Comparisons of numerical simulations between the trapezoidal and double S speed profiles for the three PMSMs. (a-c) Control voltages. (d-f) Angular displacements. (g-i) Angular speeds. (T: trapezoidal speed profile; S: double S speed profile)

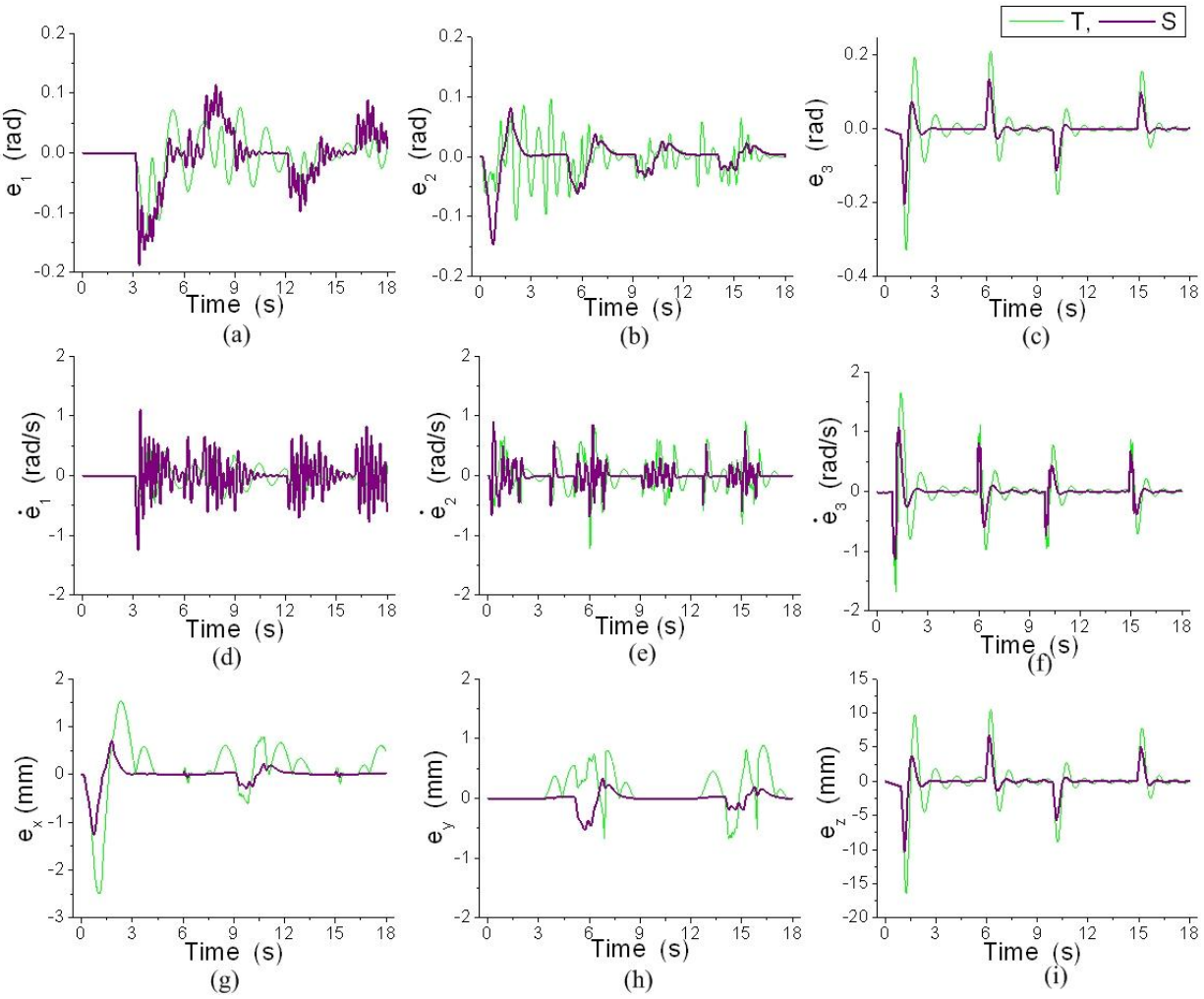

Figure 8. Comparisons of numerical simulations between the trapezoidal and double S speed profiles. (a-c) Angular-displacement errors of PMSMs. (d-f) Angular-speed errors of PMSMs. (g-i) The position errors in the *x*-axis, y-axis and z-axis of Arm3, respectively. (T: trapezoidal speed profile; S: double S speed profile)

Moreover, Figure 8 shows the comparison of response errors between the trapezoidal and double S speed profiles. Figures 8(a-c) show the angular-displacement errors of the three PMSMs, and it is seen that the double S speed profile is more suitable than the trapezoidal speed profile. Figures 8(d-f) show the angular-speed errors of the PMSMs, while Figures 8(g-i) show the position error s in the *x*-, *y*- and *z*- axis for the Arm 3.

Figures 9(a-o) show comparisons between numerical simulations and experimental results of the proposed adaptive controller in controlling the 3-DOF LCD glass-handling robot system. In this case, external loading and unknown disturbance are not considered in the numerical simulations, but are considered in the experimental setup. In experiments, the constant vectors and constant values are taken as follows:

$$\gamma_1 = [100\times10^{-4} \quad 5\times10^{-4} \quad 3\times10^{-4}],$$
$$\gamma_2 = [20\times10^{-4} \quad 80\times10^{-4} \quad 1\times10^{-4}],$$
$$\gamma_3 = [50\times10^{-4} \quad 60\times10^{-4} \quad 5\times10^{-4}],$$
$$\gamma_4 = [10\times10^{-4} \quad 40\times10^{-4} \quad 1\times10^{-4}],$$
$$\boldsymbol{h} = diag(h_1, h_2, h_3) = diag(10,15,5),$$
$$\lambda = diag(0.85,0.7,0.75), \text{ and } D = 100.$$

Figures 9(a-c) show control voltages and it is seen that the experimental values are larger than those of numerical simulations. Figures 9(d-f) and Figures 9(j-l) show the angular displacements and their corresponding errors, respectively, in numerical simulations and experimental results. Figures 9(g-i) and Figures 9(m-o) show the angular speed and their corresponding errors, respectively, and it is seen that the experimental errors are larger than those of numerical simulations. It is noted that only the angular displacements are obtained by encoders, and the angular speeds in experiments are obtained by time differentiating the angular displacements through numerical manipulations.

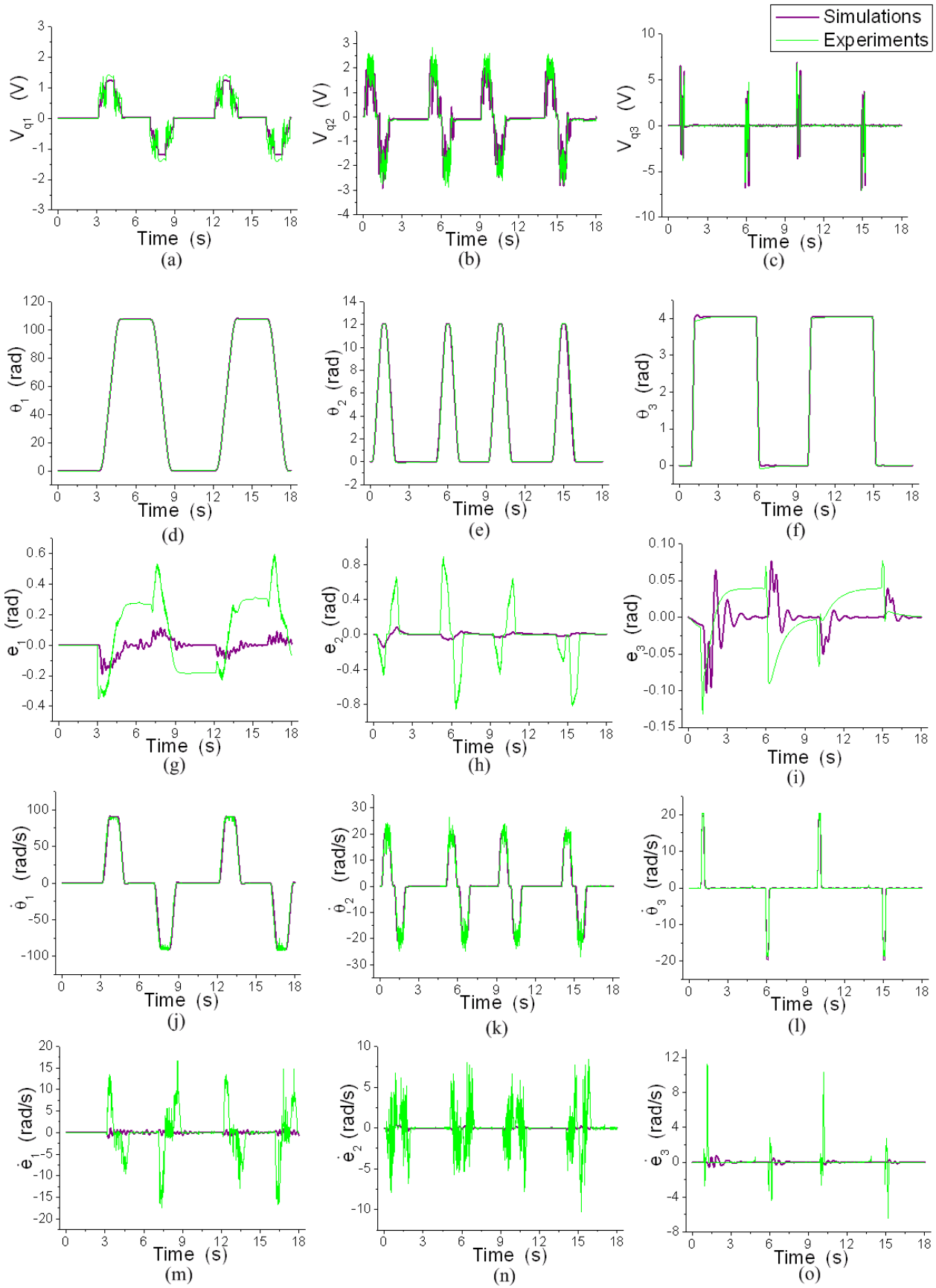

Figure 9. Comparisons between the numerical simulations and experimental results for the three PMSMs. (a-c) Control voltages. (d-f) Angular displacements. (g-i) Angular-displacement errors. (j-l) Angular speeds. (m-o) Angular-speed errors.

Conclusion

One main objective for this study is to formulate the dynamic mechatronic equations including the electrical and mechanical equations. The RGA method was employed to identify the parameters of a 3-DOF LCD glass-handling robot, and the errors are all below 1.5 %. From these results it is validated that the RGA method is feasible for the mechatronic system. The proposed adaptive control scheme was presented with unknown parametric uncertainties and disturbances, and then used to control the robot system to track the designed trajectories for comparisons in numerical simulation and experimental results. From these comparisons, since the trapezoidal speed command generates large jumping in the turning points, it was determined that the double S speed trajectory is therefore more suitable for the robot system.

Acknowledgment

The financial support from National Science Council of the Republic of China with contract number NSC-97-2221-E-327-016-MY3 is gratefully acknowledged.

References

[1] R. F. Fung, Y. S. Kung, and G. C. Wu, "Dynamic analysis and system identification of an LCD glass-handling robot driven by a PMSM," *Applied Mathematical Modelling,* vol. 34, no. 5, pp. 1360-1381, 2010. doi: 10.1016/j.apm.2009.08.020

[2] R. F. Fung, Y. L. Hsu, and M. S. Huang, "System identification of a dual-stage xy precision positioning table," *Precision Engineering,* vol. 33, no. 1, pp. 71-80, 2009. doi: 10.1016/j.precisioneng.2008.04.002

[3] R. F. Fung and W. C. Lin, "System identification of a novel 6-DOF precision positioning table," *Sensors and Actuators A: Physical,* vol. 150, no. 2, pp. 286-295, 2009. doi: 10.1016/j.sna.2009.01.007

[4] L. Tian and C. Collins, "An effective robot trajectory planning method using a genetic algorithm," *Mechatronics,* vol. 14, no. 5, pp. 455-470, 2004. doi: 10.1016/j.mechatronics.2003.10.001

[5] Y. L. Hsu, M. S. Huang, and F. Rong-Fong, "Adaptive tracking control of a toggle mechanism for the electric injection molding machines," in *29th Chinese Control Conference (CCC)*, Beiging, China, 2010, pp. 2212-2218.

[6] L. Biagiotti and C. Melchiorri, *Trajectory planning for automatic machines and robots*, 1st ed. Berlin Heidelberg: Springer-Verlag, 2008.

[7] Q. Hu, G. Ma, and L. Xie, "Robust and adaptive variable structure output feedback control of uncertain systems with input nonlinearity," *Automatica,* vol. 44, no. 2, pp. 552-559, 2008. doi: 10.1016/j.automatica.2007.06.024

[8] R. Shahnazi and M. R. Akbarzadeh-T, "PI adaptive fuzzy control with large and fast disturbance rejection for a class of uncertain nonlinear systems," *IEEE Transactions on Fuzzy Systems,* vol. 16, no. 1, pp. 187-197, 2008. doi: 10.1109/TFUZZ.2007.903320

[9] C. W. Chuang, M. S. Huang, K. Y. Chen, and R. F. Fung, "Adaptive vision-based control of a motor-toggle mechanism: Simulations and experiments," *Journal of Sound and Vibration,* vol. 312, no. 4-5, pp. 848-861, 2008. doi: 10.1016/j.jsv.2007.11.019

[10] F. J. Lin and Y. S. Lin, "A robust PM synchronous motor drive with adaptive uncertainty observer," *IEEE Transactions on Energy Conversion,* vol. 14, no. 4, pp. 989-995, 1999. doi: 10.1109/60.815018

[11] T. S. Lee, C. H. Lin, and F. J. Lin, "An adaptive H∞ controller design for permanent magnet synchronous motor drives," *Control Engineering Practice,* vol. 13, no. 4, pp. 425-439, 2005. doi: 10.1016/j.conengprac.2004.04.001

[12] R. F. Fung and W. C. Lin, "System identification and contour tracking of a plane-type 3-DOF precision positioning table," *IEEE Transactions on Control Systems Technology,* vol. 18, no. 1, pp. 22-34, 2010. doi: 10.1109/TCST.2008.2009528

[13] R. F. Fung, M. H. Weng, and Y. S. Kung, "FPGA-based adaptive backstepping fuzzy control for a micro-positioning Scott-Russell mechanism," *Mechanical Systems and Signal Processing,* vol. 23, no. 8, pp. 2671-2686, 2009. doi: 10.1016/j.ymssp.2009.01.005